Spiral Layer-by-Layer Micro-Nanostructured Scaffolds for Bone Tissue Engineering

Ohan S. Manoukian[†,‡], **Aja Aravamudhan**[†], **Paul Lee**[§], **Michael R. Arul**[†], **Xiaojun Yu**[§], **Swetha Rudraiah**[‖], and **Sangamesh G. Kumbar**[*,†,‡]

[†]Department of Orthopaedic Surgery, University of Connecticut Health, 263 Farmington Avenue, Farmington, Connecticut 06030, United States

[‡]Department of Biomedical Engineering, University of Connecticut, 260 Glenbrook Road, Unit 3247, Storrs, Connecticut 06269, United States

[§]Department of Chemistry, Chemical Biology, and Biomedical Engineering, Stevens Institute of Technology, 1 Castle Point Terrace, Hoboken, New Jersey 07030, United States

[‖]Department of Pharmaceutical Sciences, School of Pharmacy, University of Saint Joseph, 229 Trumbull St., Hartford Connecticut 06103, United States

Abstract

This Article reports the fabrication and characterization of composite micro-nanostructured spiral scaffolds functionalized with nanofibers and hydroxyapatite (HA) for bone regeneration. The spiral poly(lactic acid-*co*-glycolic acid) (PLGA) porous microstructure was coated with sparsely spaced PLGA nanofibers and HA to enhance surface area and bioactivity. Polyelectrolyte-based HA coating in a layer-by-layer (LBL) fashion allowed 10–70 μM Ca^{2+}/mm^2 incorporation. These scaffolds provided a controlled release of Ca^{2+} ions up to 60 days with varied release kinetics accounting up to 10–50 μg. Spiral scaffolds supported superior adhesion, proliferation, and osteogenic differentiation of rat bone marrow stromal cells (MSCs) as compared to controls microstructures. Spiral micro-nanostructures supported homogeneous tissue ingrowth and resulted in bone-island formation in the center of the scaffold as early as 3 weeks in a rabbit ulnar bone defect model. In contrast, control cylindrical scaffolds showed tissue ingrowth only at the surface because of limitations in scaffold transport features.

[*]**Corresponding Author** Phone: (860) 679-3955. Fax: (860) 679-1553. kumbar@uchc.edu.

1. INTRODUCTION

Scaffold-based tissue engineering strategies have shown great promise as a viable alternative to traditional methods, such as autografts and allografts, for the repair of lost or damaged bone tissue.[1] The relative ease and feasibility of fabrication, functionalization, sterilization, and commercialization has contributed greatly to the interest of using bone graft substitutes or scaffolds for such applications. Such advantages enable tissue engineering scaffolds the ability to overcome limitations of current, traditional treatments including donor site morbidity, immunogenicity, and disease transmission.[2,3] Particularly for bone applications, osteoconductive, osteoinductive, and osteointegrative properties are often incorporated to more efficiently promote bone regeneration.[4]

Recent studies have shown the importance of incorporating both micro and nanostructured elements on the performance of bone tissue engineering (BTE) scaffolds.[4–8] However, the fusion of micro and nanostructures for tissue regeneration scaffolds still remains a tremendous challenge, as it can result in decreased scaffold performance or ultimately scaffold failure if the composite structures are not brought together in a seamless and complementary manner.[6] Nanohydroxyapatite (nano-HA or HA) is gaining new impetus in the field of BTE, owing to the innovations in material fabrication resulting in distinctive biomechanical properties. Nano-HA crystals ($Ca_{10}(PO_4)_6(OH)_2$) constitute the chief inorganic component of mineral bone in a very well-defined spatial and hierarchical orientation to collagen fibrils.[9]

In general, HA offers key properties such as biocompatibility, surface grain size, favorable topography, and porosity. Thus, HA materials produce excellent osteoconduction and subsequent matrix mineralization, which is often considered as the rate-limiting process of bone healing at large defect gaps.[10] The dissolution of HA releases inorganic calcium and phosphateions and results in the reprecipitation of crystals, therefore enhancing the process of biomineralization in vivo.[11] It is well established that the supplementation of calcium and phosphate facilitates collagen biomineralization.[12] In addition, nano-HA has been shown to possess unique properties due to its nanosize regime and quantum confinement, including significant increases in protein adsorption and osteoblast adhesion.[13] To date, several preparation methodologies have been studied for the integration of HA or other ceramics into scaffolds including blending for nanofiber spinning,[11,14] phase separation,[15,16] and plasma deposition[17] on to the surface for improved osteoconductivity. Most of these incorporation techniques inherit several shortcomings including gravity settling (phase separation) of the ceramics and uneven distribution in three-dimensional (3D) scale, directly correlated with HA concentration. These factors regularly result in non-homogeneous and inconsistent HA loading into the scaffold architecture.[18]

It is believed that nanostructured polymeric fibers facilitate the adsorption of selective proteins due to high surface area-to-volume ratio leading to enhanced cell adhesion and osteogenic differentiation.[16,19] Several studies were able to demonstrate that scaffolds composed of nanofibrous configurations were able to enhance osteogenic differentiation compared to flat materials of the same composition.[20] The nanostructured networks of polymeric fibers provide ample porosity for nutrient diffusion, gas/metabolic waste exchange, as well as vascularization and cell penetration which are all features of key tenets ineffective osteoinduction and osteoconduction.[21–25] Furthermore, they can enable the delivery of macromolecules, growth factors, and various small molecule drugs.[7,25–28] However, polymeric nanofibers lack the mechanical integrity to properly mimic and reproduce native tissue and often result in scaffolding with inherit mismatch in their mechanical properties. To combat this, most commonly reported biomimetic scaffolds are porous, cylindrical, or tubular in structure.[29–32] In spite of many merits including interconnected porosity and mechanical strength, these macro-structured scaffolds often fail to allow adequate cellular infiltration into the core of the scaffolds. The closed architecture design of these scaffolds only permits limited cell penetration to a depth of 200–800 μm and inadequate nutrient influx, especially impacting the core of the scaffolds.[33] It is hypothesized that modification of scaffold configuration may ensure improved cellular penetration, nutrient transport, media influx and metabolic waste exchange resulting in enhanced cell-matrix interaction and phenotype maturation.[34]

To address the aforementioned challenges and shortcomings, we report the design, fabrication, and testing of a novel, bioinspired, spiral-shaped scaffold configuration comprised of polymeric nanofibers and uniformly deposited porous nano-scale HA for superior osteoinduction and matrix mineralization. We have optimized current HA incorporation techniques for a uniform deposition of HA onto a nanofiber-based spiral structure and evaluated its ability to support the differentiation of mesenchymal stem cells into osteoblasts throughout the scaffold structure. A polyelectrolyte-based layer-by-layer (LBL) self-assembly technique was applied to homogeneously deposit HA throughout the scaffold. LBL deposition is a versatile and effective technology based on electrostatic interactions between oppositely charged polymers and coordinative interactions or hydrogen bonds for the purpose of fabricating multiple ultrathin layers of various materials.[35]

The main advantages of this applied LBL methodology are 3-fold: first, it allows for the ability to uniformly deposit bioceramics on the scaffold surface, instead of the core; second, to accurately control the film growth rate at the nanometer scale; third, to modify the surface characteristics including roughness, hydrophilicity, and surface charge for the aim of improved functional osteogenesis. In the present study, we deposited five HA-polymer layers onto the scaffold surface and through the thickness to depths of 100–200 nm, thus allowing cell interactions throughout the deposited multilayers. Traditionally, it has been challenging to control the thickness and quantity of HA adsorption when using HA-polymer blends. With the applied LBL self-assembly methodology, we report superior control of the thickness and quantity of HA adsorption in nanoscale resolution, not only on the surface, but throughout the multilayer depth, for improved cell-material interaction.[36]

2. MATERIALS AND METHODS

Poly(lactic acid-*co*-glycolic acid) (PLGA, 85:15) was purchased from Lakeshore Biomaterials (Birmingham, AL). Poly(vinyl alcohol) (PVA) (MW = 30–70 kDa), polyethylenimine (PEI), tannic acid, alizarin red, acetylpyridinium chloride, dichloromethane, and ethanol were purchased from Sigma-Aldrich (St. Louis, MO). Hydroxyapatite 50–500 nm was purchased from Berkeley Advanced Biomaterials (San Leandro, CA). Primary rat bone marrow stromal cells (BMSCs) were acquired from Lonza (Allendale, NJ), expanded as per supplier's protocol and used at passage 4. All cell culture supplies including cell culture media, trypsin, fetal bovine serum, and penicillin/streptomycin were purchased from Invitrogen (Carlsbad, CA). Electrospinning setup was custom built for in-house applications utilizing a voltage source from Gamma Electric (Orlando, FL).[37]

2.1. PLGA Microparticles Synthesis and Spiral Scaffold Preparation.

PLGA microparticles were synthesized using traditional oil in water (o/w) emulsion techniques as described previously.[7,38] A 10% solution of PLGA was made in dichloromethane and was added to a water phase containing 1% solution of PVA. The solution was stirred using an overhead stirrer at a rate of 350 rpm for 3 h until all the solvent evaporated. The formed microparticles were vacuum filtered and triple washed to remove remaining PVA and were dried in a vacuum desiccator overnight. The microparticles were then sieved, to separate them by size, and particles in the size range of 100–200 μm were used for scaffold preparation. The scaffold preparation procedure and the nanofiber coating procedures have been described in detail in our earlier publications.[7,39] Briefly, the PLGA microspheres were sintered together to form a thin film sheet, upon which PLGA nanofibers were deposited via electrospinning.[7,10] The thin film strips were then rolled up to form the spiral architecture scaffolds presented in this study. The spiral scaffolds presented in this study measured 5 mm in diameter and 5 mm in height. The wall thickness was 500 μm and the gap between two successive walls was 1 mm.

2.2. Control Scaffolds.

Cylindrical control scaffolds were prepared using identical aforementioned sintering techniques as used for the preparation of spiral scaffolds.[40] The cylindrical scaffolds had the same diameter and height dimensions as that of spiral scaffolds, and only lacked the spiral architecture. The cylindrical scaffolds were fabricated via salt leaching, where 25% salt was added prior to sintering and then leached out for 48 h prior to application.

2.3. Layer-by-Layer Deposition of Hydroxyapatite.

HA was deposited onto PLGA scaffolds using a polyelectrolyte LBL process. PLGA has a slightly negative charge at all pH values, which aided in the deposition of positively charged (cationic) polyethylenimine (PEI) (0.5 mg/mL, pH 4.0) as the primary, base layer. The PEI coats the surface of the PLGA scaffolds and induces uniform positive charge on the surface. The scaffolds were then thoroughly washed in deionized (DI) water and air-dried prior to deposition of the subsequent layers. A tannic acid solution (1 mg/mL, pH 2.0) was blended with HA (1% w/v, 50–500 nm particles) to form a uniform, anionic, HA solution prior to

deposition. Because of charge exclusion, the HA stayed suspended in the medium during deposition. Prior to deposition of the following cationic layer, the scaffolds were washed thoroughly using DI water three times, followed by the deposition of chitosan (2 mg/mL, pH 2.0). The scaffolds were washed again in DI water and the deposition steps of HA and chitosan were repeated to form bilayers containing HA (Figure 1). Five bilayers of anionic and cationic polymers (HA and chitosan, respectively) were deposited and compared against 0, 1, and 3 bilayers. For appropriate controls, HA was deposited on cylindrical scaffolds as well as the spiral scaffolds without nanofiber coating.

2.4 Quantification of Hydroxyapatite Deposited on Scaffolds.

To determine the amount of HA deposited onto the bilayer coated spiral scaffolds, an alizarin red based colorimetric assay was used. Control scaffolds (without HA) and scaffolds containing 1, 3, and 5 bilayers of HA were dipped in a 1% aqueous solution of alizarin red for 1 min. The scaffolds were then thoroughly washed with DI water and imaged using a Nikon inverted microscope (Nikon Instruments, Inc., Melville, NY). The alizarin red which attached to the calcium ions was solubilized in a 10% solution of cetylpyridinium chloride, until all the red color was dissolved. 150 μL of this solution was transferred to a 96 well plate and the absorbance was measured a wavelength corresponding to 562 nm. All samples were tested in triplicate ($n = 5$). The amount of calcium deposited was quantified based on a standard calibration curve obtained by measuring the absorbance of varying concentrations of a $CaCl_2$ solution.

2.5 Calcium Ion Release.

In addition to alizarin red, calcium ion release was quantified using a total calcium assay, Stanbio Total Calcium LiquiColor (Stanbio Laboratory, Boerne, TX). Briefly, calcium is disassociated from proteins in an acid solution followed by its direct reaction with ortho-cresolphthalein complexone. The purple color formed by the complex is measured at 550 nm against a reagent blank. The amount of calcium in the sample is proportional to the color development in the complex and can be quantified using a standard curve, as per manufacturer's instructions.

2.6 Cell Seeding and Culture.

Primary rat bone marrow stromal cells (BMSCs) were used for preliminary evaluation of cell response on the nanofibrous spiral scaffolds coated with HA via LBL self-assembly technique. BMSCs at passage 4 were isolated, expanded, and characterized as per well-established protocols in previous publications.[7,41–43] Cells were cultured in culture medium comprised of Dulbecco's Modified Eagle Medium (DMEM) high glucose with L-glutamine, supplemented with 10% FBS and 1% penicillin-streptomycin. Cell cultures were maintained in a humidified incubator at 37 °C and 5% CO_2. Scaffolds were sterilized by soaking in 70% ethanol for 1 h, followed by three washes in sterile phosphate buffered saline (PBS) and subsequent UV irradiation for half an hour on each side (spiral shape facing up).

The scaffolds were placed in 24-well plates with one scaffold in each well. All scaffolds were thoroughly washed in fresh medium in order to hydrate the scaffolds prior to cell seeding. A 100 μL BMSC cell suspension with a cell concentration of 1×10^6 cells/mL was

dispersed evenly onto the walls of the scaffold. The samples were incubated for 2 h with a minimum medium for proper cell attachment, followed by the addition of 2 mL of osteogenic medium per well. The media was changed every 2 days and cultures were maintained for a total of 14 days. At day 1, 3, 7, and 14 the scaffolds were removed and characterized for cell proliferation, differentiation, mineralized matrix synthesis, and morphological analysis.

2.7. Cell Proliferation and Differentiation.

The cell proliferation at days 1, 3, 7, and 14 were analyzed using a standard MTS assay kit (Promega, Madison, WI), where viable cells reduce MTS tetrazolium to generate a colored formazan product, which is then quantified by measuring its absorbance at 490 nm.[44] The absorbance at 490 nm was measured using a microplate reader (Biotek, Winooski, VT) and all samples were measured in triplicate.

Osteoblast phenotype differentiation was evaluated at days 3, 7, and 14 by measuring alkaline phosphatase (ALP) activity. ALP content is indicative of early differentiation of cells toward an osteoblast lineage. Briefly, scaffolds were taken out and washed with PBS three times and then transferred to a 1 mL of 0.1% Triton X-100 solution and exposed to three cycles of freeze–thaw procedures for about 15 min each in order to extract the intracellular ALP protein. The resultant solution containing ALP was then analyzed using 1 mg/mL P-NPP (Sigma-Aldrich, St. Louis, MO) in $1\times$ diethanolamine substrate buffer as per the manufacturer's protocols. The reaction was stopped using a 2 M NaOH buffer and the absorbance of the solution at 405 nm was determined using a microplate reader for evaluating the ALP activity.[44] The results for ALP activity were normalized by the total protein amount in each well, which was determined by using the Bradford Protein assay kit (Bio-Rad Laboratories, Inc., Hercules, CA). Specifically, 150 μL sample obtained from the freeze–thaw cycles (solution used for ALP assay) was incubated with 150 μL Bradford reagent for 5 min and the absorbance at 595 nm was measured with a microplate reader.[44] Protein amount was determined by a standard curve that was established using known standard BSA solutions.

2.8. Mineralized Matrix Deposition.

Mineralized matrix deposition was quantified at days 3, 7, and 14 using alizarin red staining to quantify calcium deposition. Briefly, both control cylindrical and test spiral scaffolds were fixed with 4% formaldehyde in PBS at 4 °C for 60 min and then stained with 1% alizarin red solution for 10 min. The scaffolds were washed thoroughly three times using DI water. To quantify the calcium amount on the scaffold, the red matrix precipitate was solubilized in 10% cetylpyridinium chloride in water, and the optical density of the solution was read at 562 nm with a microplate reader.[4] The amount of calcium deposition was expressed as molar equivalent of $CaCl_2$ per scaffold. The background from the material alone was subtracted in each assay to assess cell-derived calcification on the materials.

2.9. Immunofluorescent Staining.

At day 14 and day 28, scaffold samples seeded with BMSCs were collected and prepared for immunofluorescent staining and microscopy. Primary antibodies included rabbit anti-

Collagen 1 (dilution 1:500), rabbit anti-osteopontin (dilution 1:500) (Abcam, Cambridge, MA). Cells were fixed in 4% paraformaldehyde solution pH 6.9 for 20 min at room temperature, followed by three PBS rinses. Samples were permeabilized with 0.2% Triton X-100 for 5 min at room temperature. Following PBS rinses, samples were blocked using 5% normal goat serum for 1 h at room temperature. In separate experiments, primary antibodies of the aforementioned protein markers were diluted appropriately in blocking solution and samples were allowed to incubate overnight at 4 °C. Post PBS rinses, fluorescent-labeled secondary antibody (antirabbit IgG; Abcam, Cambridge, MA) were applied for 1 h at room temperature in the dark. Following incubation, the spiral structures were viewed using a Zeiss LSM 510 Meta confocal laser scanning microscope (Carl Zeiss, Oberkochen, Germany).

2.10. Rabbit Ulnar Bone Defect.

Preliminary in vivo studies were conducted in a smaller (noncritical) bone defect size to establish the benefits of spiral structures over the cylindrical scaffolds in a rabbit ulnar defect. Histological evaluations were made to establish the differences in tissue ingrowth within the spiral structure and control cylindrical scaffold. Thirty male New Zealand White rabbits (age = 5–6 months; weight = 4.00–5 kg) were used in this study. All animals were cared for in accordance with the policies of the Federal Office of Laboratory Animal Welfare and the University of Connecticut's Institutional Animal Care and Use Committee. A 7 mm unilateral defect in the right ulna was created in each rabbit. Rabbits were randomly assigned to one of two treatment groups: (1) cylindrical or (2) spiral scaffolds.

The surgical procedure was performed as follows: Rabbits were anaesthetized using ketamine (50 mg/kg), xylazine (6 mg/kg), and acepromazine (1 mg/kg). The right forelimb was shaved, treated with betadine antibiotic ointment, and draped in a sterile manner. Upon exposure of both radial and ulnar bones, the segmental defect was created in the ulna with an oscillating saw using saline irrigation. The scaffolds were then placed into the site of the defect so that a tight fit was obtained. The wound, including muscle and subcutaneous tissues, were sutured closed using absorbable Vicryl 3–0 suture, and the skin was closed using nonabsorbable nylon 5–0 suture. The limb was wrapped with a gauze dressing and the sutures were removed approximately 7 days postoperative. Enrofloxacin (10 mg/kg) was administered for 3 days postoperative and the pain was managed using a fentanyl transdermal patch. Animals were allowed full weight-bearing activity and access to food and water.

At 10 weeks, the rabbits were sedated with acepromazine (1 mg/kg) and euthanized with a lethal dose of sodium pentobarbital (175 mg/kg). The outer skin was dissected from the forelimb with the remaining tissues were left intact. The limb was harvested by further dissection at the elbow and wrist joints and transferred to a histological container filled with 10% neutral buffered formalin and fixed at 4 °C in preparation for histological assessments. Contralateral control limbs were prepared in an identical manner. Bone samples were embedded in a plastic embedding system based on methyl methacrylate (MMA) (Electron Microscopy Sciences, Hatsfield, PA). In brief, fixed samples were dehydrated in an ascending alcohol series at room temperature. The samples were immersed in

polymerization mixture consisting of MMA and peroxide and allowed to polymerize at 4 °C for approximately 24 h in glass vials, according to manufacturer protocols. The glass vials were broken after completion of hardening and the embedded bone samples were cut using a diamond-coated saw band to thicknesses of 0.1–0.3 mm. These samples were later ground to a thickness of 6 μm in order to facilitate the evaluation of histological structures.

Following standard protocols, histological evaluations of the spiral scaffolds, namely hematoxylin and eosin (H&E) staining and Masson–Goldner trichrome staining, were performed at 3 weeks and 10 weeks postimplantation, respectively. Micro-CT three-dimensional reconstructions of the ulnar defect substituted with the scaffold were processed at 10 weeks postimplantation.

2.11. Statistical Analysis.

All quantitative data are reported as the mean ± standard deviation. A minimum of 3 samples per time point per group were evaluated for statistical analysis. All results were first evaluated using one-way analysis of variation (ANOVA) followed by Dunnett's multiple comparisons test with a confidence of 95% using GraphPad Prism 7 (GraphPad Software, Inc. La Jolla, CA).

3. RESULTS

In the two-step scaffold fabrication process, microspheres were fused together by heating above the glass transition temperature in the form of a thin sheet. The microsphere sheet was decorated with sparsely spaced nanofibers by electrospinning. Scaffolds have a uniform wall and gap architecture leading to excellent pore interconnectivity and porosities as discussed in our earlier publication.[45] The open gap, spiral architecture substantially increases surface area and allows for easy nutrient influx into the scaffolds. It was hypothesized that the porous architecture would allow for uniform deposition of ceramics on the polymer surface within the scaffold bulk. In an effort for a thorough investigation, multiple variations of scaffolds were fabricated and tested, including spiral scaffolds with zero, one, three, and five bilayers, with and without nanofibers, and cylindrical control scaffolds with adsorbed HA and aforementioned bilayers (see Figure S1 for test plan schematic). Prolonged exposure to acidic coating environment may result in polymer degradation as evidenced through literature reports.[46] However, the current coating methodology was optimized to minimize exposure to 30 min to maintain polymer integrity. Molecular weight analysis before and after coating showed no substantial changes in molecular weight, however polydispersity index changed from 1.5 to 1.7.[47]

Spiral structures were designed to replicate the porosity of human trabecular bone, which is approximately 70%. The pore sizes of both cylindrical and spiral scaffolds were expected to be similar due to the use of similar sized microspheres and sintering methodology during fabrication. The average porosity value was determined to be 90.15 ± 1.38% for spiral scaffolds and 42.02 ± 0.34% for cylindrical scaffolds, measured using mercury porosimetry, which are consistent with values in literature.[48,49] Pore sizes were determined to be in the diameter range of 165 ± 6.36 consistent with successful literary values.[50] However, once nanofiber coating was applied, pore sizes decreased slightly to 145 ± 3.36 μm.[7,47] Figure 2

shows the differences in macrostructure of spiral and cylindrical scaffolds using optical micrographs. SEM images also show the inherent porosity of sintered microsphere structures and nanofiber coating. In an effort to ensure scaffold mechanical properties were similarly tuned to those of natural bone tissue, biomimetic scaffolds were tested for mechanical properties using compressive, torsional, and flexural mechanical tests. Spiral scaffolds demonstrated a compressive modulus 270.5 ± 52.1 MPa and compressive strength 9.5 ± 1.4 MPa that are in the range of human trabecular bone.[49] Biomimetic scaffolds tested for torsional properties at a speed of 1 deg/s measured an ultimate torsional load of 0.46 ± 0.1 N·m, ultimate rotation of 0.19 ± 0.05 rad, the stiffness of 0.12 ± 0.05 N m/degree, and torsional rigidity of 585.57 ± 272.7 N·mm^2. Spiral scaffolds showed a flexural modulus of 2080.8 ± 630.6 Pa in a three-point bending test performed at a crosshead speed of 0.1 mm/s. These scaffolds reached a maximum flexural stress of 142.38 ± 10.08 N/m^2 and strain of 0.077 ± 0.004. A sample size of $n = 9$ was used for all mechanical testing studies.

Amount of HA deposited onto the surface was quantified, based on calcium absorbance, as previously described (Figure 3A). Spiral scaffolds that had no HA coating showed no absorbance at 562 nm, and the control scaffold onto which HA was applied using traditional adsorption methods, showed minimal absorbance for calcium present in the HA. This is attributed to the presence of an increased surface area of the nanofiber coating, which promoted a nominal adsorption of HA onto the polymer fibers. We deposited 0, 1, 3, and 5 HA layers sequentially, leading to a significant increase in quantified calcium, directly correlated to the number of HA layers, as compared to the traditional adsorption method. A 5-layer deposition of HA onto the surface deposited approximately 60 μM calcium/mm^2 of HA. In contrast, 3-layer deposition resulted in approximately 45 μM calcium/mm^2 of HA, 1 layer resulted in approximately 30 μM calcium/mm^2 of HA, and traditional adsorption of HA resulted in less than 20 μM calcium/mm^2.

The release profiles of calcium ions from the spiral scaffolds with 0, 1, 3, and 5 bilayers of HA deposited over 60 days are shown in Figure 3B. A burst release is observed in all three bilayer formulations within the first 3 days where 3.96%, 6.59%, and 10.22% of cumulative calcium ions are released, respectively. At 60 days, 1, 3, and 5 bilayer HA scaffolds had released 18.14%, 26.26%, and 46.72% of cumulative calcium ions, respectively.

Bone marrow stromal cells (BMSCs) were seeded onto the scaffolds from the open spiral ends. The cells were allowed to attach for 2 h, after which supplemented DMEM, aforementioned, was added. Cell attachment and proliferation was evaluated at 1, 3, 7, and 14 days postseeding using a standard MTS assay. The open architecture of spiral scaffolds significantly promoted cell attachment and proliferation, as compared to closed cylindrical scaffolds at all the time points studied (Figure 4), with nanofibers further increasing cell attachment and proliferation.

Immunofluorescent staining of BMSCs seeded on spiral scaffolds was used to show osteoblast differentiation and secretion of the bone extracellular matrix. Two primary bone extracellular matrix proteins, type I collagen and osteopontin, were stained at 14- and 28-day time points to characterize osteoblast differentiation of BMSCs. Two primary bone extracellular matrix proteins, type I collagen and osteopontin, were stained at 14- and 28-day

time points to characterize osteoblast differentiation of BMSCs. Figure 5A and 5B show the secretion of type I collagen (stained green) by differentiated BMSCs (stained blue) at day 14 and day 28, respectively. A clear abundance of type I collagen secretion can be observed at both time points within the spiral scaffold structure. Similarly, Figure 5C and 5D show the secretion of osteopontin (stained green) by differentiated BMSCs (stained blue) at day 14 and day 28, respectively. The expression of both osteogenic markers, namely, collagen I and osteopontin, was uniform throughout the spiral scaffold architecture.

The differentiation of stem cells and their ability to form bone-like matrix was further evaluated by measuring the alkaline phosphatase (ALP) activity. Proliferating osteoblasts show ALP activity, which is greatly enhanced during in vitro bone formation.[51] The observed behavior of the differentiated stem cells was very similar to that reported in primary osteoblasts.[13,16,52,53] The phenotypic expression profile confirms early differentiation of the cells and was evaluated at days 3, 7, and 14. Enhanced ALP activity was measured on open spiral scaffold structures and spiral scaffolds with nanofibers as shown in Figure 6. As hypothesized, a significant increase in ALP activity was observed on the nanofiber-coated spiral scaffolds, compared to cylindrical scaffolds, which is indicative of the enhanced differentiation potential and the combinatorial effect of nanofibers and HA in this novel scaffold design. Similar to the cell attachment and proliferation results of the MTS assay shown previously in Figure 4, the hierarchy of ALP performance between scaffolds remained consistent, with cylindrical scaffolds showing the least ALP activity, followed by spiral scaffolds, and finally spiral-nanofiber-HA hybrid as the best performing, with the greatest ALP activity.

As a final characterization of osteoblast differentiation and integration within the LBL spiral scaffolds, matrix mineralization was tested. Mineralization was examined using a colorimetric alizarin red assay based on the quantification of solubilized red matrix precipitate using cetylpyridinium chloride solution, as previously described. Quantification studies demonstrated that calcium deposition was significantly enhanced in spiral scaffolds and nanofibrous spiral scaffolds (Figure 7), as compared to cylindrical control scaffolds.

A rabbit ulnar bone defect model was utilized to demonstrate the efficacy of the LBL spiral scaffolds for osteoblast differentiation, integration, and bone regeneration in vivo. A 5×7 mm rabbit ulnar defect was substituted with a spiral scaffold with 5 bilayers of HA deposited via LBL technique. Ten weeks postimplantation, the microCT 3D reconstruction (Figure 8A and 8B) of spiral scaffold repair reveals far superior regeneration of bone in both anterior and posterior views of the ulnar defect. The cylindrical scaffold repair shows a clear, vast section of bone that has not regenerated or repaired within 10 weeks.

PMMA embedded, alcian blue stained sections of the scaffolds at 3 weeks postimplantation revealed new bone formation throughout the spiral scaffolds. Control cylindrical scaffolds, presented in Figure 9A, shows substantially decreased the formation of osteocytic cells as compared to spiral scaffold structure shown in Figure 9B. The blue staining indicative of glycosaminoglycans (GAGs) and hence showing the presence of a cartilage to bone transition along with the osteocyte cell structure in the spiral structures shown in Figure 9B, 9D, and 9F are absent in the control cylindrical structures are seen in Figure 9A, 9C, and 9E.

Furthermore, cross sections of the spiral scaffold sample indicate a clear formation of a new bone "island" in the central interior of the scaffold (Figure 10B), a distinct feature of bone formation visibly lacking in control cylindrical scaffold samples. In contrast, Figure 10A shows a longitudinal section of the cylindrical scaffold, presenting cellular infiltration (Figure 10A, 10C, and 10E) without an osteoblastic morphology as seen in the spiral structures (Figure 10B, 10D, and 10F). The substantial bone formation can be seen in the middle of the spiral scaffolds (substantial bone formation can be seen in the middle of the spiral scaffolds (Figures 9B and 10B), a challenging feat for many bone tissue-engineering scaffolds. The dense matrix content in the spiral structures indicates a collagenous extracellular matrix arranged in particular helical order. Small islets of bony matrix were detected at the inner parts of the scaffold indicated osteoblastic differentiation. Differentiated osteoblasts can be seen localized at the margin of the trabeculae as lining cells (dark red-brown color). Such findings indicate a regulated process of bone formation.

4. DISCUSSION

Previously, HA-based ceramic approaches have been attempted to create and reconstruct bone; however, these attempts have led to suboptimal results because of poor, nonhomogeneous HA loading, sporadic and inconsistent calcium release, and slow resorption rates.[18,54] Unlike traditional HA coatings and encapsulation strategies, which create a rough nanotopography, uneven distribution, and nonuniform depth of distribution, the LBL approach provides alternate layers of polymer coating which ensures a smoother surface, as compared to traditional deposition techniques. As such, the approach presented in this study may be advantageous for cellular adhesion, proliferation, differentiation, and integration not only on a biological level but also due to its physical topographical micro-nanostructure. The proper incorporation and dissolution of HA are critical as it releases inorganic calcium and phosphate ions and results in the reprecipitation of crystals, therefore, enhancing the process of biomineralization in vivo.[11]

Using the LBL strategy, HA is coated on the surface of the scaffold, allowing for better cell-extracellular matrix interactions, which improved the regenerative capability of the scaffold.[55,56,57,58] The strong cationic nature of PEI encourages initial polyelectrolyte layer formation for coating sintered PLGA scaffolds, as evidenced by literature reports.[57,58] Despite PEI being described as having an acceptable degree of biocompatibility,[57] minor toxicity concerns were reported when PEI-based biomaterials were used. However, in the current study, cells were not directly in contact with PEI as it was further coated with multiple layers of chitosan. Chitosan has been shown to have a high ability to form polyelectrolyte complexes with PEI, owing to the shapes of their titration curves.[59] Deposition of HA onto the surface of traditional scaffolds has been challenging because of the limited exposed surface area and lack of open architecture, which hinders the flow of ceramic solution into the scaffold depth. The spiral, open architecture allows for improved cellular infiltration and cell adhesion, which has been challenging in the case of closed cylindrical scaffolds. The nanofiber coating on the scaffold enhanced surface area thereby improving the HA attachment to the surface, which showed a marked difference in scaffold performance in vitro.[60,61] The polyelectrolyte LBL deposition allowed for controlled, reproducible incorporation of HA, which was shown to achieve the predictable and highly

tunable release of calcium ions.[62] We hypothesize that the enhanced matrix deposition is due to the promotion of cell-biomimetic scaffold interactions arising due to the uniform surface coating of ceramics throughout the scaffold, as compared to the alternative, blend systems where HA is deposited largely within the composite scaffold.

Various publications report the optimal level of HA loading on the surface of titanium implants to be 45–70 μM calcium/mm^2 for excellent osteoinduction.[2,3] A 5-layer deposition of HA onto the surface of the presented spiral nanofiber scaffolds deposited approximately 60 μM calcium/mm^2 of HA, which would provide an optimal HA density sufficient to induce differentiation of osteoblast cells, enhance host-scaffold interactions, and improve osteoconduction. This LBL process was shown to be tunable and a direct correlation was shown between a number of layers and calcium absorption.[63] As such, the technique can be modified to deposit the appropriate number of HA layers to achieve the desired concentration of calcium. In contrast to the high levels of calcium absorbed using LBL, traditional adsorption of HA resulted in less than 20 μM calcium/mm^2, which is not only suboptimal according to literature findings, but also less than the amount of calcium quantified when only 1 layer of HA was deposited using our approach.[64,62]

Cell attachment and proliferation was shown to be significantly greater on spiral scaffolds than control cylindrical scaffolds with significant enhancement of matrix mineralization and ALP production. Cells showed greater integration and infiltration into and throughout the spiral scaffolds as compared to the cylindrical scaffolds, which agrees with our initial hypothesis supporting the open architecture of the spiral design.[65] The importance of the nanofiber coating is highlighted as spiral scaffolds with nanofibers showed greater cell attachment and proliferation, ALP activity, and calcium deposition than all other groups.[65,66] Cylindrical scaffolds with and without HA were outperformed by all other groups including the raw spiral scaffold structure without the inclusion of nanofibers or HA (Figures S5–S7). Scaffolds coated with HA show enhanced cellular attachment, as compared to all other scaffolds of similar types without the incorporation of HA.[67,68] The cell proliferation data is indicative of the biocompatibility and increased cellular adhesion on the polymers having a uniform HA coating. The increase of cell adhesion and proliferation with time and the greatest cell proliferation of BMSCs at day 14 on the hybrid nanofiber-HA scaffold attributes to the individual advantages of spiral structures, nanofibers, and uniform multilayer HA coating, as well as the combinatorial advantages of the composite spiral scaffold, compared to the various control scaffolds. Similar results with ALP activity and calcium deposition further support this claim.

Immunofluorescent staining showed positive expression for type I collagen and osteopontin at multiple time points on and within spiral scaffolds. The mineralized extracellular matrix (ECM) is composed of two types of proteins: the collagens and the noncollagenous proteins. The collagens, mostly Type I Collagen, account for 90% of the bone matrix proteins.[52,69] Noncollagenous proteins including osteopontin, osteocalcin, matrix GLA protein, and bone sialoprotein make up bone ECM in smaller, but significant amounts.[53] The positive staining of two primary bone ECM proteins indicates successful differentiation of BMSCs seeded on the LBL spiral scaffold into osteoblast lineage. Furthermore, as evidenced by the cross-sectional images presented in Figure 9, where the faint blue color represents the scaffold

structure, differentiated BMSCs were able to infiltrate throughout the depth of the LBL spiral scaffold and secrete ECM proteins within the interior of the structure.

The efficacy of the spiral scaffolds to repair and regenerate bone was evaluated in rabbit ulnar defect models. were evaluated in rabbit ulnar defect models. in vivo were evaluated in rabbit ulnar defect models.[70] The extent of healing and quality of the regenerated tissue were significantly different between spiral and cylindrical scaffolds. Defects substituted with LBL HA spiral scaffolds allowed substantial osteogenesis and resulted in the significant formation of new bone and repair, with distinct bone island formation as early as 3 weeks. In contrast, defects substituted with cylindrical scaffolds displayed large sections, especially in the interior of the structure, with fibroblastic cellular morphology including tissue that had minimal GAG and collagen content. An abundance of collagenous and GAG matrix formation observed in spiral scaffold sections is evidence to the structure's superior regeneration capabilities, compared to cylindrical scaffolds, where cellular activity was shown to be considerably decreased and limited to the scaffold surface.[50,71]

While most BTE scaffold structures (i.e., conventional cylindrical structures) allow for tissue infiltration, bone formation, particularly at the core of the BTE material, is difficult to achieve. The spiral structured implants allowed for dense bone formation at the core of the scaffold due to their superior osteoconductive nature owing to the greater space achieved by the structures, which facilitated infiltration of osteoblastic cells. Furthermore, the effective incorporation of osteoinductive HA into these materials was also conducive for rendering the material osteoinductive toward progenitor cells, attributing to greater bone healing.

This study has left open the question as to whether the osteosynthesis and newly-formed bone elicited an appropriate the stress–strain pattern and stress transfer along the tissue engineering bone. Mechanical stresses play a critical role in determining the architecture of bone and bone is often remodeled in response to mechanical loading via mechano-transduction.[72] Although the results shown suggest spiral HA scaffolds facilitate osteoblast differentiation and active in vivo bone formation, the mechanical compliance of newly formed bone is uncertain. As such, future studies will evaluate the mechanical behavior of the regenerated bone compared to the native bone in order to determine its mechanical efficacy and compliance as an alternative to current bone repair methods.

5. CONCLUSIONS

Bioceramics, in particular, HA, have been widely used for BTE applications due to their biocompatibility and osteoconductive properties. Several notable challenges exist with composites of HA for BTE scaffolds, most notably compromised properties, nonuniform distribution, and ion release irregularities due to phase separation at higher HA content. This study investigated the fabrication and characterization of the polymeric porous, spiral micro-nanostructured scaffolds, functionalized with nanofibers and LBL deposition of HA, and evaluated their ability to support bone regeneration.

In summary, the LBL hydroxyapatite spiral structures performed better than all other scaffolds tested, confirming the advantages of both a unique HA deposition technique and a

spiral structure for bone regeneration. Our findings demonstrate that high surface area, achieved by the spiral structure and nanofiber incorporation, in conjunction with high HA-loading efficiencies, granted by the unique polyelectrolyte LBL deposition technique, allow for the controlled release of calcium ions and osteoblastic differentiation in vitro and efficient bone matrix formation in vivo, eliciting true bone regeneration capabilities.

Supplementary Material

Refer to Web version on PubMed Central for supplementary material.

ACKNOWLEDGMENTS

REFERENCES

(1). Barrere F; Mahmood T; De Groot K; Van Blitterswijk C Advanced biomaterials for skeletal tissue regeneration: Instructive and smart functions. Mater. Sci. Eng., R 2008, 59 (1), 38–71.

(2). Ito H; Koefoed M; Tiyapatanaputi P; Gromov K; Goater JJ; Carmouche J; Zhang X; Rubery PT; Rabinowitz J; Samulski RJ; Nakamura T; Soballe K; O'Keefe RJ; Boyce BF; Schwarz EM Remodeling of cortical bone allografts mediated by adherent rAAV- RANKL and VEGF gene therapy. Nat. Med. 2005, 11 (3), 291–7. [PubMed: 15711561]

(3). De Long WG Jr.; Einhorn TA; Koval K; McKee M; Smith W; Sanders R; Watson T Bone grafts and bone graft substitutes in orthopaedic trauma surgery. A critical analysis. J. Bone Joint Surg Am. 2007, 89 (3), 649–58. [PubMed: 17332116]

(4). Aravamudhan A; Ramos DM; Nip J; Harmon M; James R; Deng M; Laurencin CT; Yu X; Kumbar SG Cellulose and Collagen Derived Micro-Nano Structured Scaffolds for Bone Tissue Engineering. J. Biomed. Nanotechnol. 2013, 9, 719–731. [PubMed: 23621034]

(5). Woodard JR; Hilldore AJ; Lan SK; Park C; Morgan AW; Eurell JAC; Clark SG; Wheeler MB; Jamison RD; Wagoner Johnson A. J. The mechanical properties and osteoconductivity of hydroxyapatite bone scaffolds with multi-scale porosity. Biomaterials 2007, 28 (1), 45–54. [PubMed: 16963118]

(6). Brown JL; Peach MS; Nair LS; Kumbar SG; Laurencin CT Composite scaffolds: bridging nanofiber and microsphere architectures to improve bioactivity of mechanically competent constructs. J. Biomed. Mater. Res., Part A 2010, 95 (4), 1150–1158.

(7). Lee P; Manoukian OS; Zhou G; Wang Y; Chang W; Yu X; Kumbar SG Osteochondral scaffold combined with aligned nanofibrous scaffolds for cartilage regeneration. RSC Adv. 2016, 6 (76), 72246–72255.

(8). James R; Deng M; Laurencin CT; Kumbar SG Nanocomposites and bone regeneration. Frontiers of Materials Science 2011, 5 (4), 342–357.

(9). Landis WJ; Silver FH Mineral deposition in the extracellular matrices of vertebrate tissues: identification of possible apatite nucleation sites on type I collagen. Cells Tissues Organs 2008, 189 (1–4), 20–4. [PubMed: 18703872]

(10). Kumbar SG; Nukavarapu SP; James R; Nair LS; Laurencin CT Electrospun poly(lactic acid-co-glycolic acid) scaffolds for skin tissue engineering. Biomaterials 2008, 29 (30), 4100–4107. [PubMed: 18639927]

(11). Teng S-H; Lee E-J; Wang P; Kim H-E Collagen/hydroxyapatite composite nanofibers by electrospinning. Mater. Lett. 2008, 62 (17–18), 3055–3058.

(12). Chang YL; Stanford CM; Keller JC Calcium and phosphate supplementation promotes bone cell mineralization: implications for hydroxyapatite (HA)-enhanced bone formation. J. Biomed. Mater. Res. 2000, 52 (2), 270–8. [PubMed: 10951365]

(13). Webster TJ; Ergun C; Doremus RH; Siegel RW; Bizios R Specific proteins mediate enhanced osteoblast adhesion on nanophase ceramics. J. Biomed. Mater. Res. 2000, 51 (3), 475–483. [PubMed: 10880091]

(14). Venugopal J; Low S; Choon AT; Sampath Kumar T. S.; Ramakrishna S Mineralization of osteoblasts with electrospun collagen/hydroxyapatite nanofibers. J. Mater. Sci.: Mater. Med. 2008, 19 (5), 2039–46. [PubMed: 17957448]

(15). Huang YX; Ren J; Chen C; Ren TB; Zhou XY Preparation and properties of poly(lactide-co-glycolide) (PLGA)/nano-hydroxyapatite (NHA) scaffolds by thermally induced phase separation and rabbit MSCs culture on scaffolds. J. Biomater. Appl. 2008, 22 (5), 409–32. [PubMed: 17494961]

(16). Woo KM; Jun JH; Chen VJ; Seo J; Baek JH; Ryoo HM; Kim GS; Somerman MJ; Ma PX Nano-fibrous scaffolding promotes osteoblast differentiation and biomineralization. Biomaterials 2007, 28 (2), 335–43. [PubMed: 16854461]

(17). Xu S; Long J; Sim L; Diong CH; Ostrikov K RF Plasma Sputtering Deposition of Hydroxyapatite Bioceramics: Synthesis, Performance, and Biocompatibility. Plasma Processes Polym. 2005, 2 (5), 373–390.

(18). Tahmasbi Rad A.; Solati-Hashjin M; Osman NAA; Faghihi S Improved bio- physical performance of hydroxyapatite coatings obtained by electrophoretic deposition at dynamic voltage. Ceram. Int. 2014, 40 (8), 12681–12691.

(19). Ripamonti U The induction of bone in osteogenic composites of bone matrix and porous hydroxyapatite replicas: an experimental study on the baboon (Papio ursinus). J. Oral Maxillofac Surg 1991, 49 (8), 817–30. [PubMed: 1649284]

(20). Smith LA; Liu X; Hu J; Ma PX The enhancement of human embryonic stem cell osteogenic differentiation with nano-fibrous scaffolding. Biomaterials 2010, 31 (21), 5526–35. [PubMed: 20430439]

(21). Manoukian O; Ahmad A; Marin C; James R; Mazzocca A; Kumbar S Bioactive nanofiber dressings for wound healing. Wound Healing Biomaterials-Volume 2: Functional Biomaterials 2016, 451.

(22). Blakeney BA; Tambralli A; Anderson JM; Andukuri A; Lim DJ; Dean DR; Jun HW Cell infiltration and growth in a low density, uncompressed three-dimensional electrospun nanofibrous scaffold. Biomaterials 2011, 32 (6), 1583–90. [PubMed: 21112625]

(23). Manoukian OS; Nip J; Abiola O; Gopalakrishna A; Kumbar SG Tissue-Engineered Medical Products. Biomaterials and Nanotechnology for Tissue Engineering 2016, 289.

(24). Baker BM; Gee AO; Metter RB; Nathan AS; Marklein RA; Burdick JA; Mauck R L. The potential to improve cell infiltration in composite fiber-aligned electrospun scaffolds by the selective removal of sacrificial fibers. Biomaterials 2008, 29 (15), 2348–58. [PubMed: 18313138]

(25). Manoukian OS; Matta R; Letendre J; Collins P; Mazzocca AD; Kumbar SG Electrospun Nanofiber Scaffolds and Their Hydrogel Composites for the Engineering and Regeneration of Soft Tissues. Methods Mol Biol. 2017, 1570, 261–278. [PubMed: 28238143]

(26). James R; Manoukian OS; Kumbar SG Poly (lactic acid) for delivery of bioactive macromolecules. Adv. Drug Delivery Rev. 2016, 107, 277–288.

(27). Sridhar R; Lakshminarayanan R; Madhaiyan K; Amutha Barathi V.; Lim KHC; Ramakrishna S Electrosprayed nanoparticles and electrospun nanofibers based on natural materials: applications in tissue regeneration, drug delivery and pharmaceuticals. Chem. Soc. Rev. 2015, 44 (3), 790–814. [PubMed: 25408245]

(28). Li L; Zhou G; Wang Y; Yang G; Ding S; Zhou S Controlled dual delivery of BMP- 2 and dexamethasone by nanoparticle-embedded electrospun nanofibers for the efficient repair of critical-sized rat calvarial defect. Biomaterials 2015, 37, 218–229. [PubMed: 25453952]

(29). Schliephake H; Knebel JW; Aufderheide M; Tauscher M Use of cultivated osteoprogenitor cells to increase bone formation in segmental mandibular defects: an experimental pilot study in sheep. Int. J. Oral Maxillofac Surg 2001, 30 (6), 531–7. [PubMed: 11829236]

(30). Gutierres M; Lopes MA; Sooraj Hussain N.; Lemos AF; Ferreira JM; Afonso A; Cabral AT; Almeida L; Santos JD Bone ingrowth in macroporous Bonelike for orthopaedic applications. Acta Biomater. 2008, 4 (2), 370–7. [PubMed: 17716960]

(31). Matsumoto K; Ohnishi K; Kiyotani T; Sekine T; Ueda H; Nakamura T; Endo K; Shimizu Y Peripheral nerve regeneration across an 80-mm gap bridged by a polyglycolic acid (PGA)-collagen tube filled with laminin-coated collagen fibers: a histological and electrophysiological evaluation of regenerated nerves. Brain Res. 2000, 868 (2), 315–28. [PubMed: 10854584]

(32). Aravamudhan A; Ramos DM; Nip J; Kalajzic I; Kumbar SG Micro- Nanostructures of Cellulose-Collagen for Critical Sized Bone Defect Healing. Macromol Biosci. 2018, 18, 1700263.

(33). Ishaug-Riley SL; Crane GM; Gurlek A; Miller MJ; Yasko AW; Yaszemski MJ; Mikos AG Ectopic bone formation by marrow stromal osteoblast transplantation using poly(DL-lactic-co-glycolic acid) foams implanted into the rat mesentery. J. Biomed. Mater. Res. 1997, 36 (1), 1–8. [PubMed: 9212383]

(34). Yoshimoto H; Shin YM; Terai H; Vacanti JP A biodegradable nanofiber scaffold by electrospinning and its potential for bone tissue engineering. Biomaterials 2003, 24 (12), 2077–2082. [PubMed: 12628828]

(35). Michel M; Toniazzo V.r; Ruch D; Ball V. Deposition Mechanisms in Layer-by-Layer or Step-by-Step Deposition Methods: From Elastic and Impermeable Films to Soft Membranes with Ion Exchange Properties. ISRN Materials Science 2012, 2012, 1.

(36). Yao X; Peng R; Ding J Cell–Material Interactions Revealed Via Material Techniques of Surface Patterning. Adv. Mater. 2013, 25 (37), 5257–5286. [PubMed: 24038153]

(37). Nada AA; James R; Shelke NB; Harmon MD; Awad HM; Nagarale RK; Kumbar SG A smart methodology to fabricate electrospun chitosan nanofiber matrices for regenerative engineering applications. Polym. Adv. Technol 2014, 25 (5), 507–515.

(38). Manoukian OS; Arul MR; Sardashti N; Stedman T; James R; Rudraiah S; Kumbar SG Biodegradable polymeric injectable implants for long-term delivery of contraceptive drugs. J. Appl. Polym. Sci 2018, 135 (14), 46068. [PubMed: 29430061]

(39). James R; Toti US; Laurencin CT; Kumbar SG Electrospun Nanofibrous Scaffolds for Engineering Soft Connective Tissues. Methods Mol. Biol. 2011, 726, 243–258. [PubMed: 21424454]

(40). Wang J; Valmikinathan CM; Liu W; Laurencin CT; Yu X Spiral-structured, nanofibrous, 3D scaffolds for bone tissue engineering. J. Biomed. Mater. Res., Part A 2010, 93A (2), 753–762.

(41). Cheng Y; Ramos D; Lee P; Liang D; Yu X; Kumbar SG Collagen functionalized bioactive nanofiber matrices for osteogenic differentiation of mesenchymal stem cells: bone tissue engineering. J. Biomed. Nanotechnol 2014, 10 (2), 287–298. [PubMed: 24738337]

(42). Lee P; Tran K; Zhou G; Bedi A; Shelke NB; Yu X; Kumbar SG Guided differentiation of bone marrow stromal cells on co-cultured cartilage and bone scaffolds. Soft Matter 2015, 11 (38), 7648–7655. [PubMed: 26292727]

(43). Ciofani G; Ricotti L; Canale C; D'Alessandro D; Berrettini S; Mazzolai B; Mattoli V Effects of barium titanate nanoparticles on proliferation and differentiation of rat mesenchymal stem cells. Colloids Surf. B 2013, 102, 312–320.

(44). Kumbar SG; Toti US; Deng M; James R; Laurencin CT; Aravamudhan A; Harmon M; Ramos DM Novel mechanically competent polysaccharide scaffolds for bone tissue engineering. Biomed. Mater. (Bristol, U. K.) 2011, 6 (6), 065005.

(45). Nukavarapu SP; Kumbar SG; Brown JL; Krogman NR; Weikel AL; Hindenlang MD; Nair LS; Allcock HR; Laurencin CT Polyphosphazene/nano- hydroxyapatite composite microsphere scaffolds for bone tissue engineering. Biomacromolecules 2008, 9 (7), 1818–1825. [PubMed: 18517248]

(46). Fu K; Pack DW; Klibanov AM; Langer R Visual evidence of acidic environment within degrading poly (lactic-co-glycolic acid)(PLGA) microspheres. Pharm. Res. 2000, 17 (1), 100–106. [PubMed: 10714616]

(47). Aravamudhan A; Ramos D; Jenkins N; Dyment N; Sanders M; Rowe D; Kumbar S Collagen nanofibril self-assembly on a natural polymeric material for the osteoinduction of stem cells in vitro and biocompatibility in vivo. RSC Adv. 2016, 6 (84), 80851–80866.

(48). Teixeira S; Fernandes H; Leusink A; Van Blitterswijk C; Ferraz M; Monteiro F; De Boer J In vivo evaluation of highly macroporous ceramic scaffolds for bone tissue engineering. J. Biomed. Mater. Res. Part A 2010, 93 (2), 567–575.

(49). Bose S; Roy M; Bandyopadhyay A Recent advances in bone tissue engineering scaffolds. Trends Biotechnol. 2012, 30 (10), 546–554. [PubMed: 22939815]

(50). Murphy CM; Haugh MG; O'Brien FJ The effect of mean pore size on cell attachment, proliferation and migration in collagen–glycosaminoglycan scaffolds for bone tissue engineering. Biomaterials 2010, 31 (3), 461–466. [PubMed: 19819008]

(51). Kasperk C; Wergedal J; Strong D; Farley J; Wangerin K; Gropp H; Ziegler R; Baylink DJ Human bone cell phenotypes differ depending on their skeletal site of origin. J. Clin. Endocrinol. Metab. 1995, 80 (8), 2511–2517. [PubMed: 7629252]

(52). Sila-Asna M; Bunyaratvej A; Maeda S; Kitaguchi H; Bunyaratavej N Osteoblast differentiation and bone formation gene expression in strontium-inducing bone marrow mesenchymal stem cell. Kobe Journal of Medical Sciences 2007, 53 (1–2), 25–35. [PubMed: 17579299]

(53). Stein GS; Lian JB, Molecular mechanisms mediating developmental and hormone- regulated expression of genes in osteoblasts In Cellular and Molecular Biology of Bone; Academic, New York, 1993; pp 47–95.

(54). Kadiyala S; Jaiswal N; Bruder SP Culture-expanded, bone marrow-derived mesenchymal stem cells can regenerate a critical-sized segmental bone defect. Tissue Eng. 1997, 3 (2), 173–185.

(55). Guda T; Walker JA; Pollot BE; Appleford MR; Oh S; Ong JL; Wenke JC In vivo performance of bilayer hydroxyapatite scaffolds for bone tissue regeneration in the rabbit radius. J. Mater. Sci.: Mater. Med. 2011, 22 (3), 647–656. [PubMed: 21287244]

(56). Prosecká E; Buzgo M; Rampichová M; Kocourek T; Kochová P; Vysloužilová L; Tvrdík D; Jelínek M; Lukáš D; Amler E Thin-layer hydroxyapatite deposition on a nanofiber surface stimulates mesenchymal stem cell proliferation and their differentiation into osteoblasts. J. Biomed. Biotechnol. 2012, 428503. [PubMed: 22319242]

(57). Zhou J; Moya S; Ma L; Gao C; Shen J Polyelectrolyte coated PLGA nanoparticles: templation and release behavior. Macromol. Biosci. 2009, 9 (4), 326–335. [PubMed: 19089871]

(58). Yang Y-W; Hsu PY-J The effect of poly (D, L-lactide-co-glycolide) microparticles with polyelectrolyte self-assembled multilayer surfaces on the cross-presentation of exogenous antigens. Biomaterials 2008, 29 (16), 2516–2526. [PubMed: 18329708]

(59). Nicu R; Bobu E; Desbrieres J Chitosan as cationic polyelectrolyte in wet-end papermaking systems. Cellulose Chemistry and Technology 2011, 45 (1), 105.

(60). Ito Y; Hasuda H; Kamitakahara M; Ohtsuki C; Tanihara M; Kang I-K; Kwon OH A composite of hydroxyapatite with electrospun biodegradable nanofibers as a tissue engineering material. J. Biosci. Bioeng. 2005, 100 (1), 43–49. [PubMed: 16233849]

(61). Peng F; Yu X; Wei M In vitro cell performance on hydroxyapatite particles/poly (L- lactic acid) nanofibrous scaffolds with an excellent particle along nanofiber orientation. Acta Biomater. 2011, 7 (6), 2585–2592. [PubMed: 21333762]

(62). Chuang HF; Smith RC; Hammond PT Polyelectrolyte multilayers for tunable release of antibiotics. Biomacromolecules 2008, 9 (6), 1660–1668. [PubMed: 18476743]

(63). Shchukin DG; Sukhorukov GB; Möhwald H Biomimetic fabrication of nanoengineered hydroxyapatite/polyelectrolyte composite shell. Chem. Mater. 2003, 15 (20), 3947–3950.

(64). Ball V; Michel M; Boulmedais F; Hemmerle J; Haikel Y; Schaaf P; Voegel JC Nucleation kinetics of calcium phosphates on polyelectrolyte multilayers displaying internal secondary structure. Cryst. Growth Des. 2006, 6 (1), 327–334.

(65). Khang D; Lu J; Yao C; Haberstroh KM; Webster TJ The role of nanometer and sub-micron surface features on vascular and bone cell adhesion on titanium. Biomaterials 2008, 29 (8), 970–983. [PubMed: 18096222]

(66). Price RL; Waid MC; Haberstroh KM; Webster TJ Selective bone cell adhesion on formulations containing carbon nanofibers. Biomaterials 2003, 24 (11), 1877–1887. [PubMed: 12615478]

(67). Deligianni DD; Katsala ND; Koutsoukos PG; Missirlis YF Effect of surface roughness of hydroxyapatite on human bone marrow cell adhesion, proliferation, differentiation and detachment strength. Biomaterials 2000, 22 (1), 87–96.

(68). Kon E; Muraglia A; Corsi A; Bianco P; Marcacci M; Martin I; Boyde A; Ruspantini I; Chistolini P; Rocca M; et al. Autologous bone marrow stromal cells loaded onto porous hydroxyapatite ceramic accelerate bone repair in critical-size defects of sheep long bones. J. Biomed. Mater. Res. 2000, 49 (3), 328–337. [PubMed: 10602065]

(69). Robey PG Bone matrix proteoglycans and glycoproteins. Principles of bone biology 2002, 1, 225–237.

(70). Wan C; He Q; Li G Allogenic peripheral blood derived mesenchymal stem cells (MSCs) enhance bone regeneration in rabbit ulna critical-sized bone defect model. J. Orthop. Res. 2006, 24 (4), 610–618. [PubMed: 16514623]

(71). Benders KE; van Weeren PR; Badylak SF; Saris DB; Dhert WJ; Malda J Extracellular matrix scaffolds for cartilage and bone regeneration. Trends Biotechnol. 2013, 31 (3), 169–176. [PubMed: 23298610]

(72). Huang C; Ogawa R Mechanotransduction in bone repair and regeneration. FASEB J. 2010, 24 (10), 3625–3632. [PubMed: 20505115]
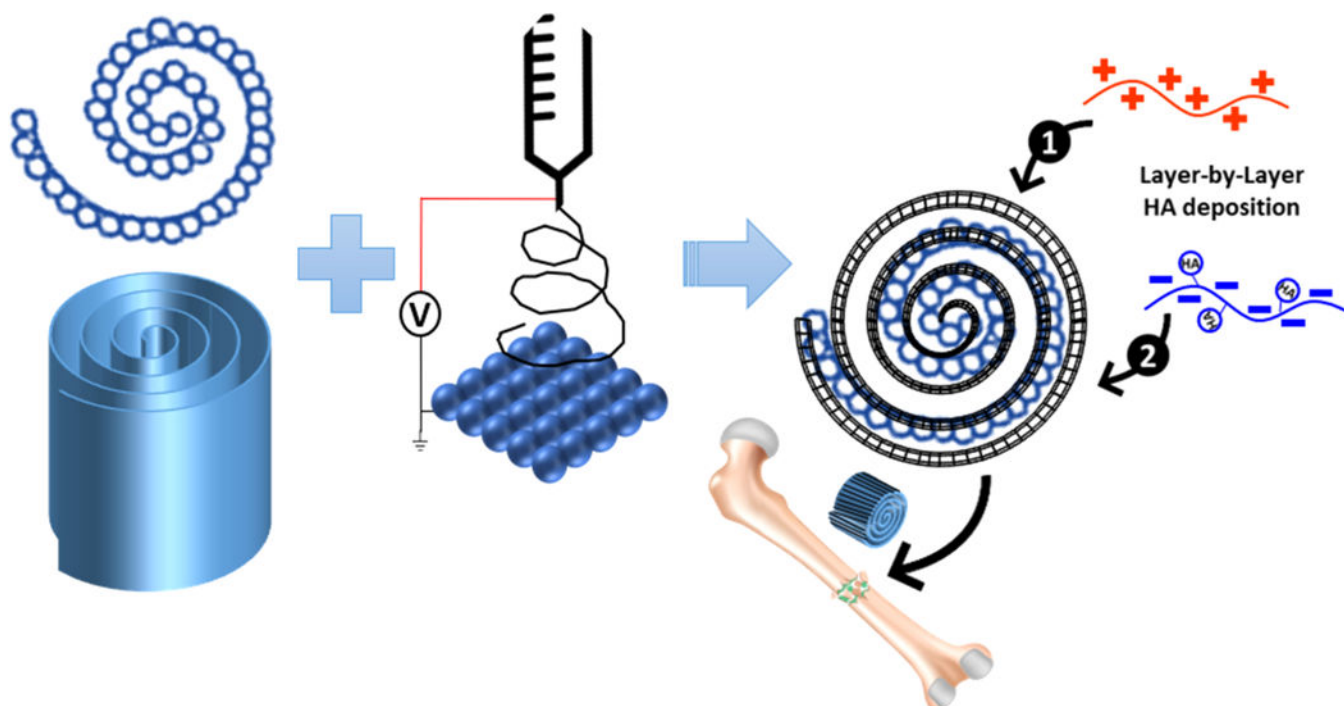
Figure 1.
Simplified schematic showing the fabrication of the sintered PLGA microsphere sheet, followed by deposition of electrospun nanofibers. The hybrid construct is then rolled into the final spiral shape. HA is deposited in a layer-by-layer polyelectrolyte process, starting with the deposition of cationic chitosan (shown in red) followed by anionic HA (shown in blue). This process is repeated to achieve desired number of HA bilayers.
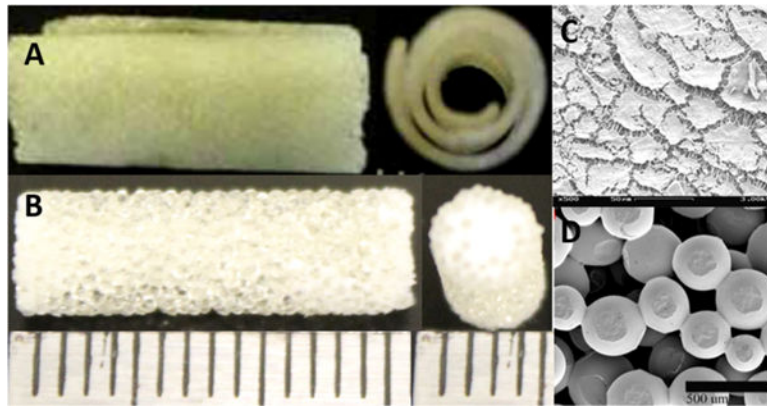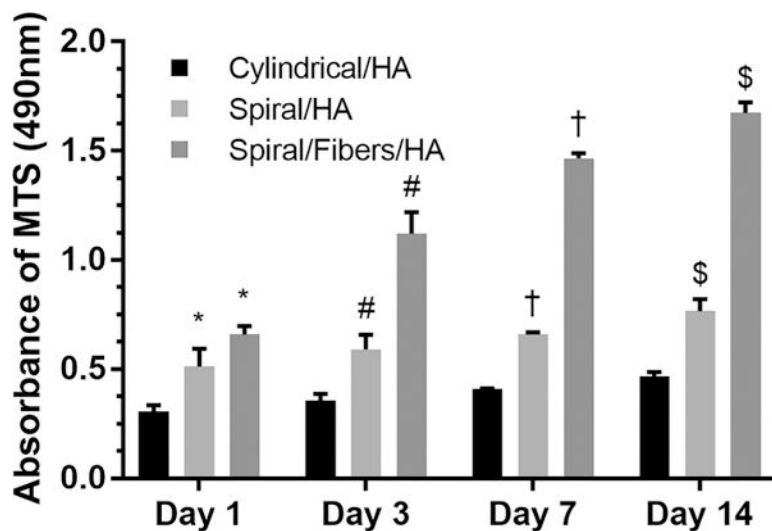
Figure 2.
(A) Optical micrograph of spiral PLGA microsphere scaffolds and (B) cylindrical PLGA microsphere scaffolds. (C) SEM showing nanofiber coating of PLGA microsphere scaffold and (D) SEM of PLGA sintered microsphere scaffolds, showing microsized pores. Both scaffolds are engineered to have identical pore properties due to similar microsphere size and sintering conditions.
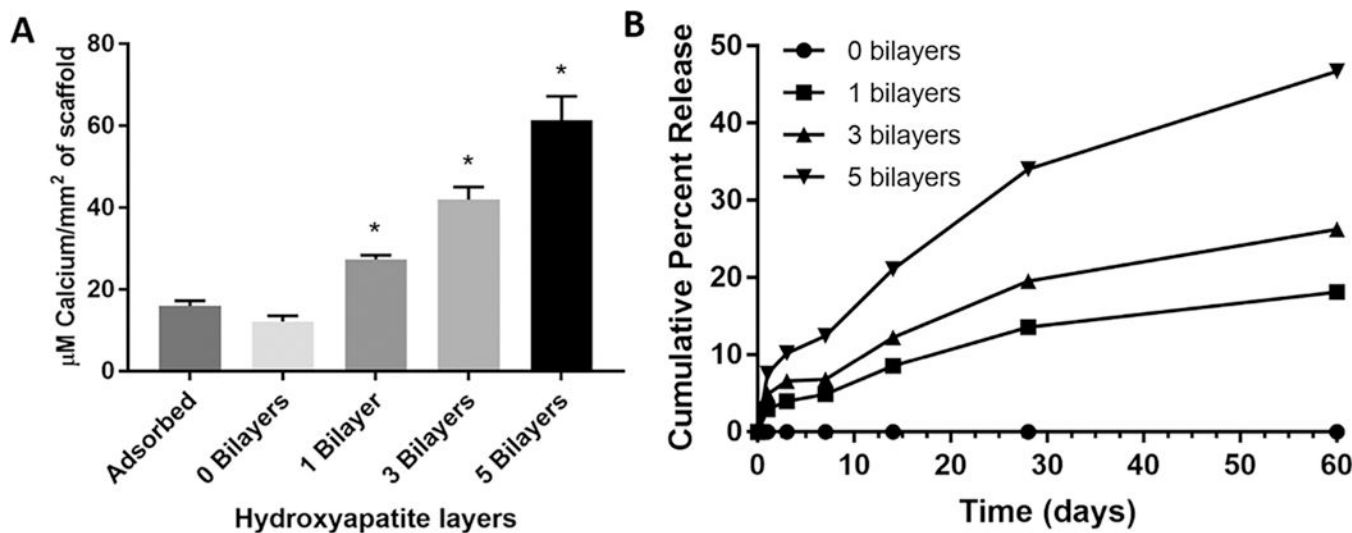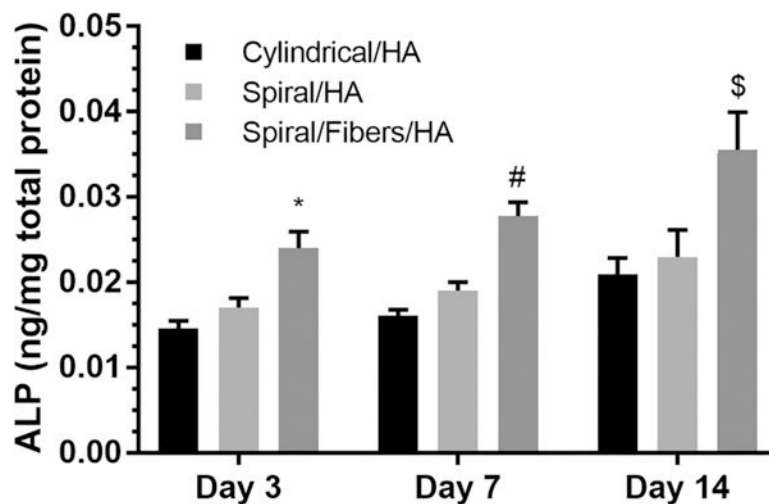
Figure 3.
(A) Quantification of calcium on spiral scaffolds with various numbers of HA bilayers deposited and control adsorbed HA. A direct correlation is shown between a number of bilayers deposited and the total calcium content on scaffolds. (B) Cumulative percent calcium ion release showing the release profiles of spiral scaffolds with 0, 1, 3, and 5 bilayers of HA deposited using the layer-by-layer technique across 60 days. An initial burst release of calcium is seen in all three bilayer scaffolds, followed by a steady, sustained release from day 7–60 with a direct correlation between a number of bilayers and the cumulative amount of calcium ions released.

Figure 4.
MTS assay showing cell attachment and proliferation on cylindrical scaffolds, spiral scaffolds, and spiral/nanofiber scaffolds. (* indicates a significant increase in cell attachment as compared to cylindrical scaffold at day 1; # indicates a significant increase in 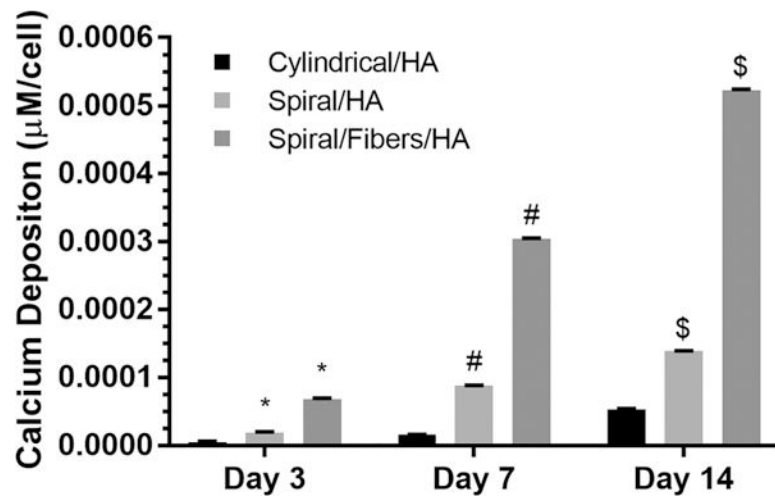cell attachment as compared to cylindrical scaffold at day 3; † indicates a significant increase in cell attachment as compared to cylindrical scaffold at day 7; $ indicates a significant increase in cell attachment as compared to the cylindrical scaffold at day 14).
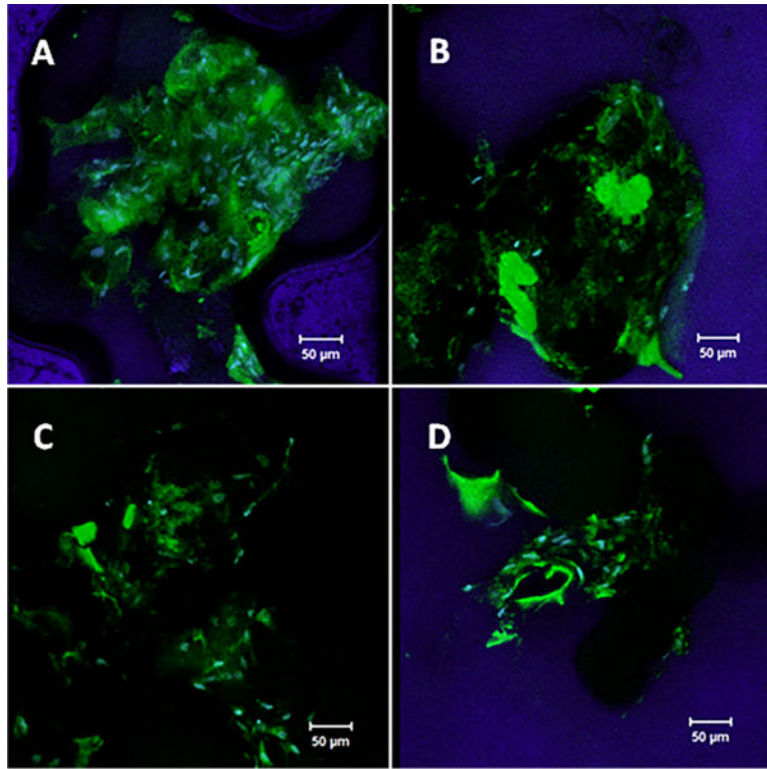
Figure 5.
Cross-sectional view of immunofluorescent staining of differentiated BMSCs seeded on and within layer-by-layer spiral scaffolds showing positive expression for (A) type I collagen at day 14, (B) type I collagen at day 28, (C) osteopontin at day 14, and (D) osteopontin at day 28.
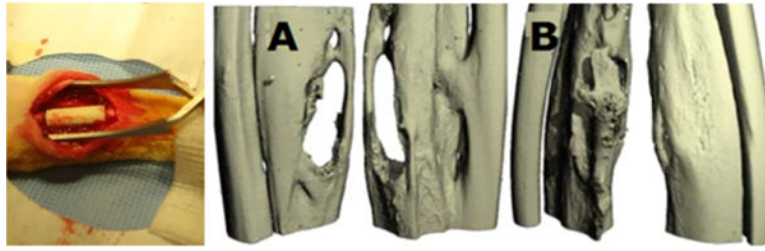
Figure 6.
Alkaline phosphatase (ALP) activity on cylindrical scaffolds, spiral scaffolds, and spiral/nanofiber scaffolds. (* indicates a significant increase in ALP as compared to the cylindrical scaffold at day 1; # indicates a significant increase in ALP as compared to the cylindrical scaffold at day 7; $ indicates a significant increase in ALP as compared to the cylindrical scaffold at day 14).
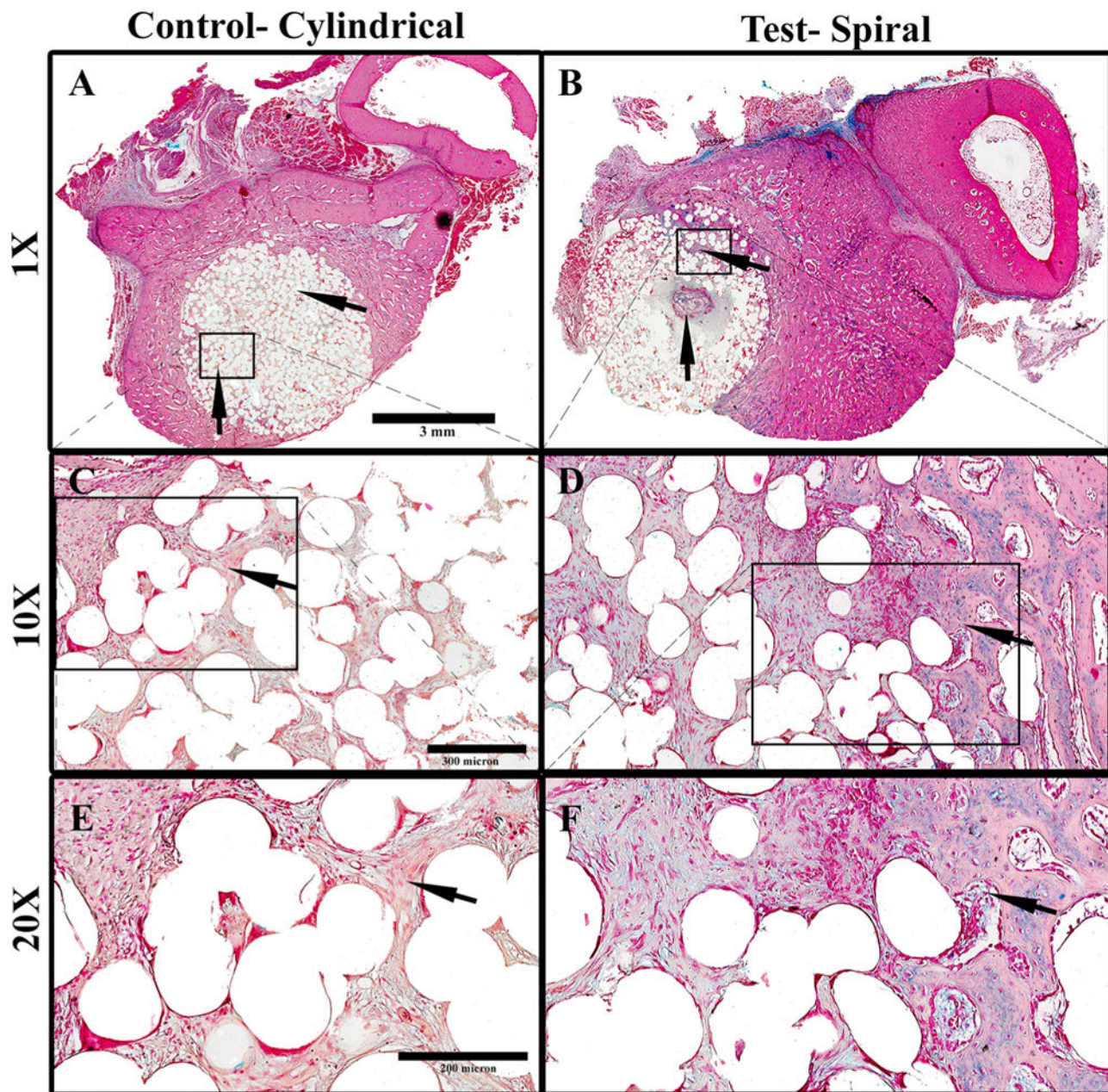
Figure 7.
Calcium deposition quantified by alizarin red assay. (* indicates a significant increase in calcium as compared to the cylindrical scaffold at day 1; # indicates a significant increase in calcium as compared to the cylindrical scaffold at day 7; $ indicates a significant increase in calcium as compared to the cylindrical scaffold at day 1).

Figure 8.
In vivo implantation of the spiral scaffold in 5 × 7 mm rabbit ulnar defect. Anterior and posterior micro-CT 3-D reconstructions at 10 weeks postimplantation showing regeneration with implanted (A) cylindrical and (B) spiral scaffolds. Spiral scaffolds showed complete regeneration of bone tissue from both anterior and posterior views.

Alcian Blue Staining- Cross Sectional View

Control- Cylindrical

Test- Spiral

Figure 9.

Cross sections of alcian blue-stained PMMA processed samples of scaffolds 3 weeks postimplantation in rabbit ulna where (A) control cylindrical scaffold (cross section 1×), (B) spiral scaffold (cross section 1×), (C) 10× magnification of A, indicating tissue infiltration, and (D) 10× magnification of B, indicating the formation of new bone in the interior of the tubular structure, (E) 20× magnification of C, indicating fibrous tissue morphology, (F) 20× magnification of D, indicating an osteocyte-like cell morphology in the interior regions of the material. Light pink-stained material indicates cellular cytoplasm and ECM surrounding

holes of the dissolved scaffold material. The cells stain deep pink and the GAG stains blue. For cylindrical scaffolds, the cells in the material's interior are more fibroblastic, with very low GAG and ECM content.
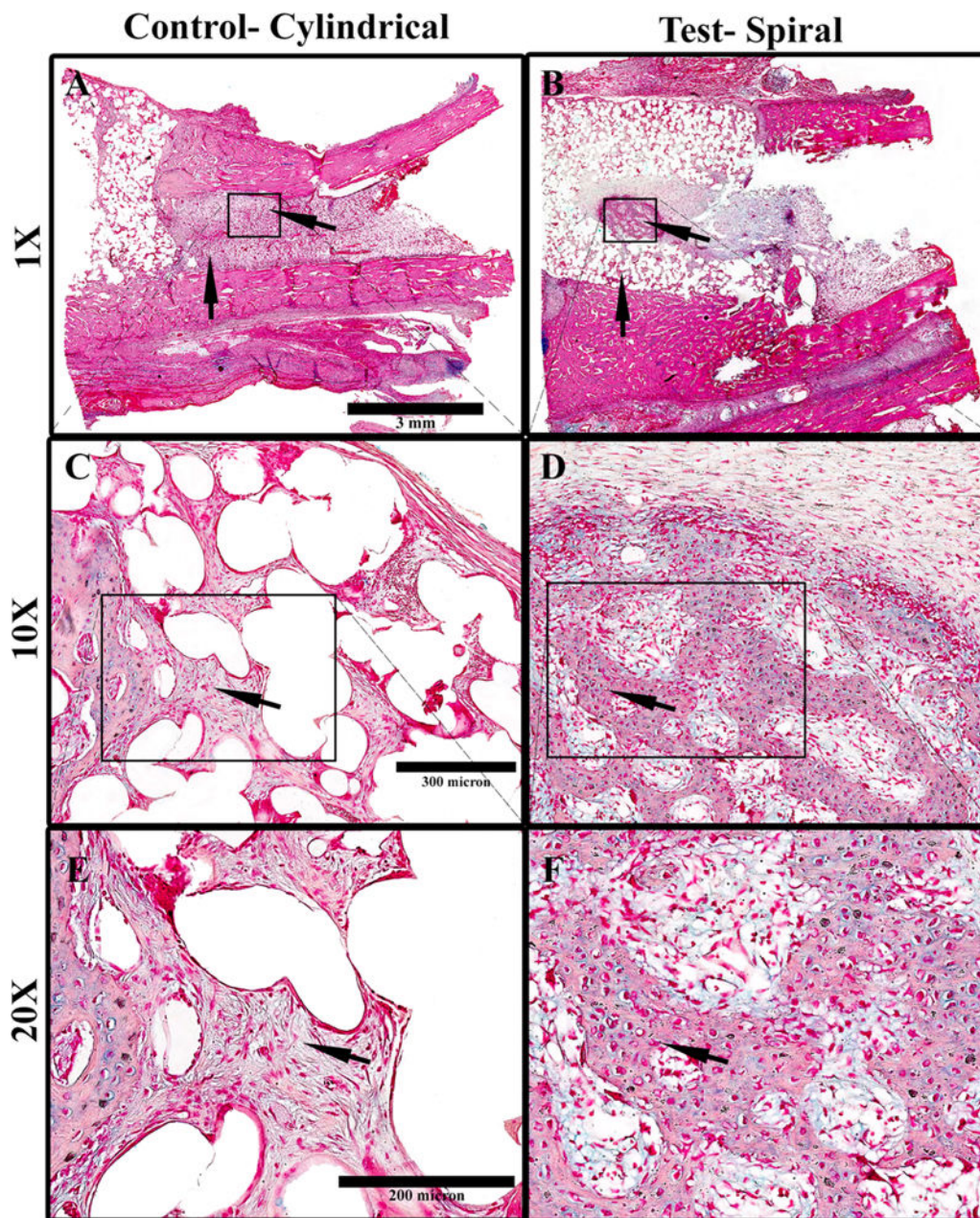
Alcian Blue Staining- Longitudanal View

Control- Cylindrical   Test- Spiral

Figure 10.
Longitudinal sections of alcian blue-stained PMMA processed samples of scaffolds, 3 weeks postimplantation in rabbit ulna where (A) control cylindrical scaffold (1×), (B) spiral scaffold (1×), (C) 10× magnification of A, indicating tissue infiltration, and (D) 10× magnification of B, indicating the formation of new bone in the interior of the tubular structure, (D) 20× magnification of C, indicating fibrous tissue morphology, (F) 20× magnification of D, indicating an osteocyte-like cell morphology in the interior regions of the material. Light Pink- stained material indicates cellular cytoplasm and ECM surrounding

holes of the dissolved scaffold material. The cells stain deep pink and the GAG stains blue. In the case of cylindrical scaffolds, the cells in the material's interior are more fibroblastic, with very low GAG and ECM content.